PNAS RESEARCH ARTICLE | EARTH, ATMOSPHERIC, AND PLANETARY SCIENCES

Carbonate uranium isotopes record global expansion of marine anoxia during the Toarcian Oceanic Anoxic Event

Mariano N. Remírez[a,1,2], Geoffrey J. Gilleaudeau[a,1,2], Tian Gan[a,b], Michael A. Kipp[c], François L. H. Tissot[d], Alan J. Kaufman[b], and Mariano Parente[e]

Affiliations are included on p. 6.

Edited by Mark Thiemens, University of California San Diego, La Jolla, CA; received March 23, 2024; accepted May 23, 2024

The Toarcian Oceanic Anoxic Event (T-OAE; ~183 Mya) was a globally significant carbon-cycle perturbation linked to widespread deposition of organic-rich sediments, massive volcanic CO_2 release, marine faunal extinction, sea-level rise, a crisis in carbonate production related to ocean acidification, and elevated seawater temperatures. Despite recognition of the T-OAE as a potential analog for future ocean deoxygenation, current knowledge on the severity of global ocean anoxia is limited largely to studies of the trace element and isotopic composition of black shales, which are commonly affected by local processes. Here, we present the first carbonate-based uranium isotope ($\delta^{238}U$) record of the T-OAE from open marine platform limestones of the southeastern Tethys Ocean as a proxy for global seawater redox conditions. A significant negative $\delta^{238}U$ excursion (~0.4‰) is recorded just prior to the onset of the negative carbon isotope excursion comprised within the T-OAE, followed by a long-lived recovery of $\delta^{238}U$ values, thus confirming that the T-OAE represents a global expansion of marine anoxia. Using a Bayesian inverse isotopic mass balance model, we estimate that anoxic waters covered ~6 to 8% of the global seafloor during the peak of the T-OAE, which represents 28 to 38 times the extent of anoxia in the modern ocean. These data, combined with $\delta^{238}U$-based estimates of seafloor anoxic area for other CO_2-driven Phanerozoic OAEs, suggest a common response of ocean anoxia to carbon release, thus improving prediction of future anthropogenically induced ocean deoxygenation.

climate change | ocean deoxygenation | ocean fertilization | Oceanic Anoxic Event

The Toarcian Oceanic Anoxic Event (T-OAE; ~183 Mya) is a carbon cycle perturbation related to the widespread deposition of organic-rich shales (1). A large negative $\delta^{13}C$ excursion (n-CIE) is embedded within the broad positive $\delta^{13}C$ excursion that characterizes the T-OAE, with this negative $\delta^{13}C$ anomaly triggered by the release of large amounts of greenhouse gases to the ocean–atmosphere system related to extensive volcanism from the Karoo–Ferrar–Chon Aike large igneous province (KFCA-LIP) (1–3). The emplacement of the KFCA-LIP is estimated to have released 20,500 Gt of carbon in seven pulses, which led to a stepwise increase in pCO_2 from ~650 ppm to ~1,700 ppm and drove a n-CIE of ~4‰ in $\delta^{13}C_{carb}$ and ~6‰ in $\delta^{13}C_{org}$ (4), with the magnitude of $\delta^{13}C$ excursions at different localities influenced by local effects (5). This global carbon cycle perturbation was linked to significant environmental changes such as an increase in seawater temperatures (6), a crisis in carbonate production (7) likely related to ocean acidification (8, 9), enhancement of the hydrological cycle (10) and weathering rates (11), enhanced marine primary productivity (12), and the expansion of marine anoxia (13, 14) that is expressed in widespread deposition of organic-rich sediments across the globe (1, 5, 15). These global biogeochemical perturbations led to substantial turnover in the marine biosphere, representing a "second-order" mass extinction characterized by a loss of ~5% of marine families (16), including major effects on ammonites, benthic foraminifera, and corals (2, 17), as well as ecological changes in belemnites (18) and ichnofossil assemblages (19).

When comparing the T-OAE with recent changes in the Earth system (and acknowledging disparities in continental configurations over time), the scale of anthropogenic impact becomes evident. In the brief span from 1850 to 2019, spanning just 169 y, human activities have contributed an estimated 2,390 ± 240 Gt of CO_2 (20)—an astonishing 12% of the entire CO_2 release observed throughout the extensive 300 to 500-kyr duration of the T-OAE n-CIE (21). This evidence underscores the accelerated pace and magnitude of contemporary CO_2 emissions, representing 12% of the T-OAE n-CIE's cumulative CO_2 release within a mere 0.035% of its duration. Thus, understanding the response of ocean anoxia to CO_2 emissions during the T-OAE n-CIE is highly relevant because CO_2

Significance

A significant negative $\delta^{238}U$ excursion (~0.4‰) starting just prior to the onset of the negative carbon isotope excursion within the Toarcian Oceanic Anoxic Event (T-OAE) has been recorded, followed by a long-lived recovery of $\delta^{238}U$ values. This excursion represents a global expansion of marine anoxia of ~6 to 8% of the global seafloor during the peak of the T-OAE, which represents 28 to 38 times the extent of anoxia in the modern ocean. When compared with estimates of seafloor anoxic area for other CO_2-driven global anoxic events, the T-OAE was the second-largest anoxic event of at least the last 300 My. As such, the T-OAE represents a powerful analog for future anthropogenic ocean deoxygenation.

Author contributions: M.N.R. and G.J.G. designed research; M.N.R., G.J.G., T.G., M.A.K., F.L.H.T., A.J.K., and M.P. performed research; M.P. contributed new reagents/analytic tools; M.N.R., G.J.G., T.G., M.A.K., F.L.H.T., A.J.K., and M.P. analyzed data; and M.N.R., G.J.G., and M.P. wrote the paper.

The authors declare no competing interest.

This article is a PNAS Direct Submission.

[1] To whom correspondence may be addressed. Email: mremirez@gmu.edu or ggilleau@gmu.edu.

[2] M.N.R. and G.J.G. contributed equally to this work.

This article contains supporting information online at https://www.pnas.org/lookup/suppl/doi:10.1073/pnas.2406032121/-/DCSupplemental.

Published June 24, 2024.

emissions during this event were comparable in magnitude to what may be expected for Earth in the coming millennia.

The n-CIE interval within the T-OAE is characterized on the North European Shelf (Cleveland, German, and Paris basins) by a $\delta^{13}C_{org}$ excursion of −5 to −7‰ and a $\delta^{13}C_{carb}$ excursion of −3 to −6‰ (5), as well as substantial local enrichment in total organic carbon (TOC) with rock TOC values normally between ~5 and 10 wt.%, reaching as high as ~17 wt.% (5, 22). However, the magnitude of the $\delta^{13}C_{org}$ and $\delta^{13}C_{carb}$ excursion through the n-CIE interval is highly variable across the rest of the Tethys Ocean and at a global scale, ranging from −0.8 to −8.6‰ and −0.6 to −6.0‰, respectively (5). In addition, relatively high TOC strata (>2.5 wt.%) are typically thought to record anoxic to euxinic (anoxic + sulfidic) local depositional conditions during the T-OAE (22), but the highest TOC strata (>5 wt.%) are only found in hydrographically restricted basins with low sedimentation rates [mostly, the North European Shelf (13, 22)], and many other basins only show a modest to negligible enrichment in TOC (5, 22). Consequently, our knowledge of the global extent of marine anoxia during the T-OAE n-CIE is derived mostly from local redox proxies applied to sections in the northern hemisphere deposited in restricted basins, challenging the global significance of marine anoxia during the T-OAE.

Transition metals and their isotopes represent powerful proxies for global redox conditions, and previous application of Mo and Tl isotopes to organic-rich mudrocks (23–26), as well as trace metal concentration modeling (14, 27) have shed light on the dynamics of ocean deoxygenation during the T-OAE. For example, low δ^{98}Mo values of euxinic shales from Europe across the T-OAE indicate expanded global ocean euxinia [~2 to 10% of the global seafloor (23)]—however, the potentially highly restricted nature of these sedimentary basins has led to challenges of this interpretation (28). Conversely, ε^{205}Tl in shales would be expected to shift to higher values associated with expanded ocean anoxia, and Canadian shales indeed exhibit two shifts to higher ε^{205}Tl values across the T-OAE interval—one beginning ~500 to 600 kyr before the onset of the n-CIE and a second, larger excursion associated with the onset of the n-CIE (25). Modeling of these Tl isotope data indicates that seafloor Mn oxide burial decreased by at least 50% during the peak T-OAE; however, Tl isotopes are not a direct proxy for seafloor anoxic area, leaving remaining uncertainties in the global extent of marine anoxia. The elemental mass balances of Re and Mo were applied to Canadian black shales to estimate anoxic and euxinic seafloor area, respectively, across the T-OAE, concluding that there was a minor expansion of seafloor anoxia preceding the n-CIE followed by a maximum of ~7% global seafloor anoxic area (dominated by euxinia) at the onset of the n-CIE (14). Although these data are robust, metal isotopes and abundances in organic-rich mudrocks are highly sensitive to local conditions, and fluctuating local redox conditions [i.e., the lack of consistent local euxinia throughout the entire studied section in Canada (14)] can introduce substantial uncertainties in interpreting global signals.

Here, we present the first complete carbonate-based uranium isotope (δ^{238}U) record across the T-OAE, providing an independent and unique constraint on global seafloor anoxic area. The δ^{238}U composition of marine carbonates has emerged as a powerful proxy for the global extent of marine anoxia (29, 30), and here we present δ^{238}U data from limestones of the Mercato San Severino section (MSS) of southern Italy (Fig. 1). These strata are part of the Apennine Carbonate Platform (ACP), which consists of a 5-km-thick pile of Upper Triassic to Upper Cretaceous shallow-water carbonates deposited at tropical latitudes on the southern margin of the Tethys Ocean. Stratigraphically, the section

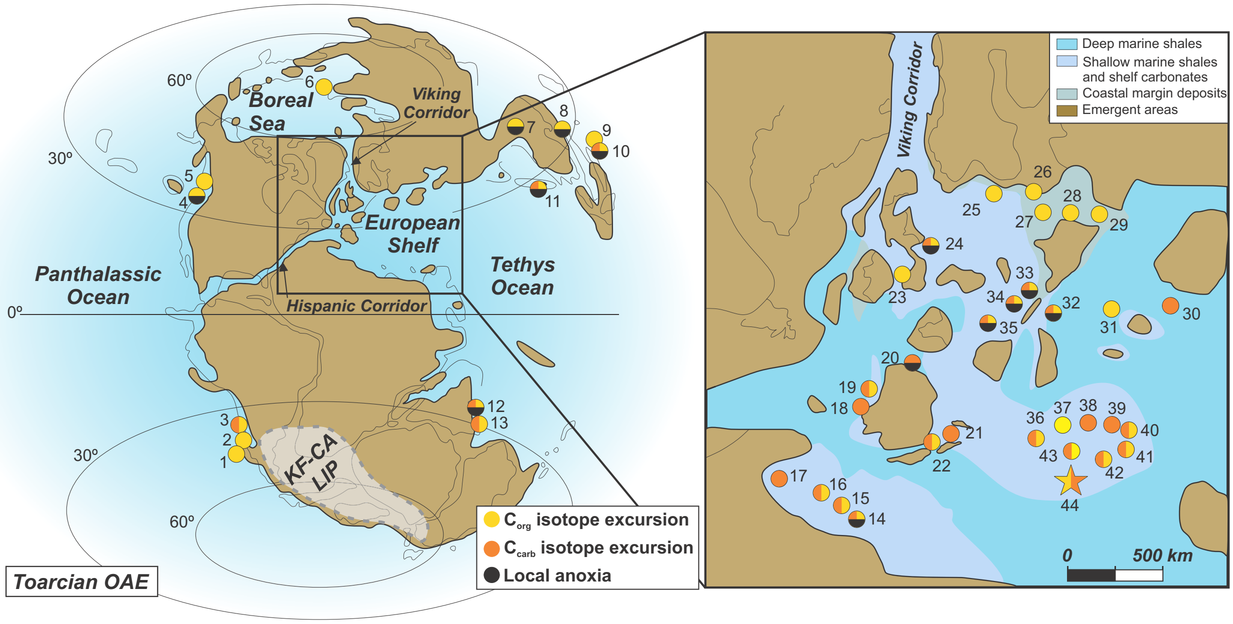

Fig. 1. Map of localities in which the T-OAE was previously recognized, along with our study site. Local anoxia refers to sites where redox proxy data reveal locally dysoxic to anoxic conditions. The site of the MSS is shown by the star in the *Inset*. KFCA-LIP: Karoo–Ferrar–Chon Aike Large Igneous Province. Sections numbered: 1: Arroyo Lapa and Arroyo Serrucho, Argentina; 2: Asientos, Chile; 3: El Peñon, Chile; 4: Haida Gwaii, Canada; 5: East Tributary of Bighorn Creek, Canada; 6: Kelimyar River, Anabar Bay, and Polovinnaya River, Russia; 7: Sichuan Core A, China; 8: Sakuraguchi-dani Valley, Japan; 9: Katsuyama, Japan; 10: Sakahogi, Japan; 11: Suobucha, China; 12: Niandou, China; 13: Wölong, China; 14: Foum Tillicht, Morocco; 15: Amellago, Morocco; 16: Boumardoul n´Imazighn, Morocco; 17: Mellala, Morocco; 18: Rabaçal, Portugal; 19: Peniche, Portugal; 20: Rodiles, Spain; 21: Es Cosconar, Spain; 22: Fuente Vidriera and La Cerradura, Spain; 23: Mochras Borehole, Wales, UK; 24: Yorkshire, England, UK; 25: Bornholm, Denmark; 26: Mechowo, Poland; 27: Gorzow Wielkpolski, Poland; 28: Kozlowice, Poland; 29: Brody-Lubienia, Poland; 30: Varbanchovets, Bulgaria; 31: Réka Valley, Hungary; 32: Creux de l´Ours, Switzerland; 33: Dotternhausen, Germany; 34: Rietheim, Switzerland; 35: Sancerre Core, France; 36: Breggia, Italy; 37: Monte Mangart, Slovenia-Italy; 38: Gornje Jelenje, Croatia; 39: Velebit A and Velebit B, Croatia; 40: Toka and Petousi, Greece; 41: Livartzki and Kastelli, Greece; 42: Monte Sorgenza, Italy; 43: Valdorbia, Italy; 44: Mercato San Severino, Italy (this study) (for references and table listing these localities, the reader is referred to *SI Appendix*).

comprises the Lower Jurassic *Palaeodasycladus* Limestones, characterized by the abundance of the calcareous alga *Palaeodasycladus mediterraneus.* The upper part of this unit is known as the Lithiotis Member, due to the large abundance of lithiotid bivalves, organized into large biostromes (31). Overlying this unit, a sharp transition leads to the deposition of the Oolitic Limestones, marked by the disappearance of the lithiotid bivalves and of *P. mediterraneus* (8). The Lithiotis Member has been interpreted as having been deposited in a very shallow marine environment in an inner platform setting, far from the platform margin (31). The Oolitic Limestones consist of very clean and well-sorted oolitic grainstones deposited in open lagoonal and marginal shoal environments. Overall, both formations represent shallow-marine carbonates, without any evidence of limited oxygen availability. While modest diagenetic alteration of uranium isotope signatures can occur in such settings (discussed below), this lithology can provide valuable insights into the uranium isotope composition of ancient seawater.

Results

In the MSS section, δ^{238}U values begin near modern carbonate values (average of −0.16‰ for the first five data points) prior to the n-CIE, followed by a sharp decline to −0.50‰ ~2 m below the onset of the n-CIE (Fig. 2). δ^{238}U values then reach a nadir of −0.62‰ at the onset of the n-CIE, followed by a progressive rise back to near-modern carbonate values over the entire course of the n-CIE. Above this, δ^{238}U values rise above modern carbonate values with an average δ^{238}U value of +0.07‰ for samples above the n-CIE. We compared our δ^{238}U data to diagenetic indicators such as δ^{18}O and Mn/Sr ratios, as well as to Mg/Ca ratios (an indicator of dolomitization) and sedimentary facies to assess any diagenetic or local depositional effects on δ^{238}U signals. Mn/Sr ratios are exceptionally low throughout the study section (<0.12), well below commonly employed diagenetic cutoff values of 2 or 10, and there is little relationship between Mn/Sr and δ^{238}U ($R^2 = 0.25$; *SI Appendix*, Figs. S1 and S2). In addition, δ^{18}O values are between −1.55‰ and −3.79‰ for the entire section (*SI Appendix*, Fig. S2), which matches global Pliensbachian–Toarcian trends (32), arguing against substantial diagenetic alteration. There is no relationship between δ^{18}O and δ^{238}U in our dataset ($R^2 = 0.10$; *SI Appendix*, Fig. S1). Mg/Ca ratios are consistently <0.05, indicating that the section has not experienced dolomitization, and U is substantially enriched above crustal values (U enrichment factors = 32 to 379 based on sample U/Al ratios compared to the upper continental crust), indicating that the majority of U in our samples originated authigenically from seawater and is not detrital in origin (*SI Appendix*, Fig. S2). In addition, the shallow-water, fossiliferous nature of the sedimentary facies indicates locally well-oxygenated conditions, which is preferable for capturing seawater δ^{238}U values without the addition of isotopically heavy authigenic U(IV) under conditions of local anoxia. There is also no clear relationship between δ^{238}U and sedimentary facies as the major negative δ^{238}U shift occurs within the Lithiotis Member and there is no change in δ^{238}U values across the transition to the overlying Oolitic Limestone. Thus, we are confident in the ability of the MSS section to record seawater δ^{238}U trends.

Discussion

Uranium in nature is dominated by two long-lived isotopes (^{235}U and ^{238}U) whose half-lives are 0.7 and 4.5 Ga, respectively. Uranium also exists in two main oxidation states: soluble U(VI) and insoluble, particle-reactive U(IV). Soluble U(VI) forms stable, unreactive calcium–uranyl–bicarbonate complexes in seawater and thus has a long residence time (~400 to 500 kyr), making it well-mixed and isotopically homogenous in the modern ocean with an isotopic composition (^{238}U/^{235}U, expressed in delta notation as δ^{238}U) of −0.379 ± 0.023‰ (33). Among various sinks for U in the ocean, the strongest isotopic fractionation is associated with removal of U to anoxic sediments, which preferentially sequester the heavier isotope ^{238}U, thereby leaving residual seawater more enriched in the lighter isotope ^{235}U. Thus, an expansion of ocean

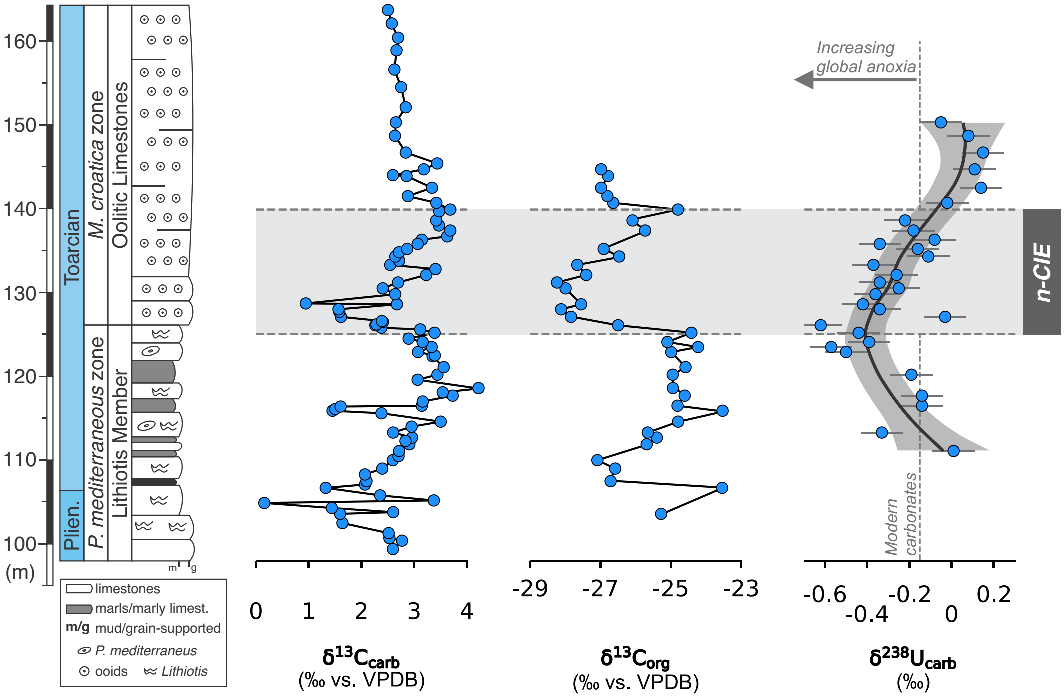

Fig. 2. Chemostratigraphy of the MSS section. This includes lithostratigraphy, biostratigraphy, sedimentological log, $\delta^{13}C_{carb}$, $\delta^{13}C_{org}$, and δ^{238}U ($\delta^{13}C_{carb}$ and $\delta^{13}C_{org}$ data from ref. 8). n-CIE = negative carbon isotope excursion within the T-OAE. LOWESS fit through δ^{238}U data was constructed using a span that minimizes the corrected Akaike Information Criterion. Optimal span was chosen to be 0.7364 and the fit was implemented in the fANCOVA R package.

anoxia will drive the δ^{238}U composition of global seawater toward lower values. Recent data suggest that substantially less fractionation occurs under ferruginous (anoxic + iron-rich) conditions (34) and suboxic conditions (35) than under euxinic conditions, and several recent studies (36, 37) found a relationship between the degree of isotopic fractionation imparted during U removal to anoxic sediments and hydrographic factors such as primary productivity and basin restriction in both euxinic and noneuxinic settings. Despite these complications, the size of the anoxic sink for U in the oceans clearly exerts the dominant control on seawater δ^{238}U values.

The δ^{238}U composition of seawater can be faithfully recorded in marine carbonate sediments under certain conditions. Modern Bahamian carbonates show a modest but consistent isotopic offset between seawater and sediment, with sediment enriched in ^{238}U on average by +0.23‰ [Bahamas median = −0.15‰ vs. seawater = −0.38‰ (33, 38, 39)]. Such positive offsets are observed at different burial depths and across different carbonate mineralogies, meaning they are pervasive but not systematic and readily correctable. Still, shifts toward lower δ^{238}U values in ancient carbonates are likely to derive from the expansion of global marine anoxia, and this relationship can be quantified with associated uncertainty using inverse isotopic mass balance modeling (40, 41).

The most parsimonious explanation for the pronounced negative δ^{238}U excursion recorded in the MSS section is that it represents a global expansion of seafloor anoxia across the T-OAE. This record represents the first independent, carbonate-based confirmation of the T-OAE as a global expansion of marine anoxia. Our record suggests that anoxic conditions predated the n-CIE, reached their peak just after the onset of the n-CIE, and recovered to well-oxygenated conditions within the course of the n-CIE. We used the most commonly accepted durations of the n-CIE [300 to 500 kyr (21)] to assign a chronology to our section based on the assumption of uniform sedimentation rates. We then applied a Bayesian inverse isotopic mass balance model (40) to the dataset to estimate seafloor anoxic area over the course of the n-CIE. We find that peak T-OAE anoxia likely represented ~6 to 8% of the global seafloor, which is 28 to 38 times greater than the modern extent of seafloor anoxia (Fig. 3). The inferred intensity of the event depends on its duration, with the shorter duration scenario (300 kyr) implying a more severe event (~8% of seafloor anoxia, with 16th to 84th percentile CI of 5 to 13%) than the longer scenario (500 kyr; ~6% of seafloor anoxia, with 16th to 84th percentile CI of 4 to 10%). These results match well with recent estimates of ~7% peak anoxic seafloor area using Re and Mo elemental mass balance models based on data from organic-rich mudrocks (14), suggesting that both shale- and carbonate-based approaches can converge on consistent estimates of seafloor anoxic area in the geologic past given optimal behavior of both shale- and carbonate-based global paleo-redox proxies.

We can also compare our results with peak seafloor anoxic areas for other Phanerozoic OAEs caused by volcanogenic CO_2 injection into the ocean–atmosphere system (Fig. 4). For example, our estimate of ~6 to 8% seafloor anoxic area for the T-OAE n-CIE is similar to δ^{238}U-based estimates of seafloor anoxic area during the LIP-induced Triassic-Jurassic boundary event (40, 42). Our estimates also suggest that the T-OAE was more severe than Cretaceous OAE 2 across the Cenomanian–Turonian boundary according to the δ^{238}U-based estimates of ref. 43, although the δ^{238}U record of ref. 44 suggests that OAE 2 had a similar magnitude as the T-OAE. Similarly, our data suggest that the T-OAE was more severe than the Paleocene–Eocene Thermal Maximum (PETM) event (40, 44). In contrast, however, the T-OAE appears to have been less severe than the Permo–Triassic boundary event (40, 45), potentially explaining the large differences in marine extinction severity between the two events. In addition, δ^{238}U data suggest that many Paleozoic OAEs [e.g., Ordovician–Silurian boundary event, Late Devonian Kellwasser and Hangenberg events (40, 46–48)] were at least as severe if not more severe than the T-OAE. In contrast to the CO_2 injection events described above, however, these Paleozoic events were characterized by carbon burial and global cooling in an atmosphere with generally lower pO_2, making them less direct analogs for future ocean deoxygenation.

Overall, results from global paleo-redox proxies such as δ^{238}U across multiple events paint a consistent picture of LIP-driven CO_2 injection to the ocean–atmosphere system causing rapid ocean deoxygenation that ultimately engulfs 5 to 10% of the

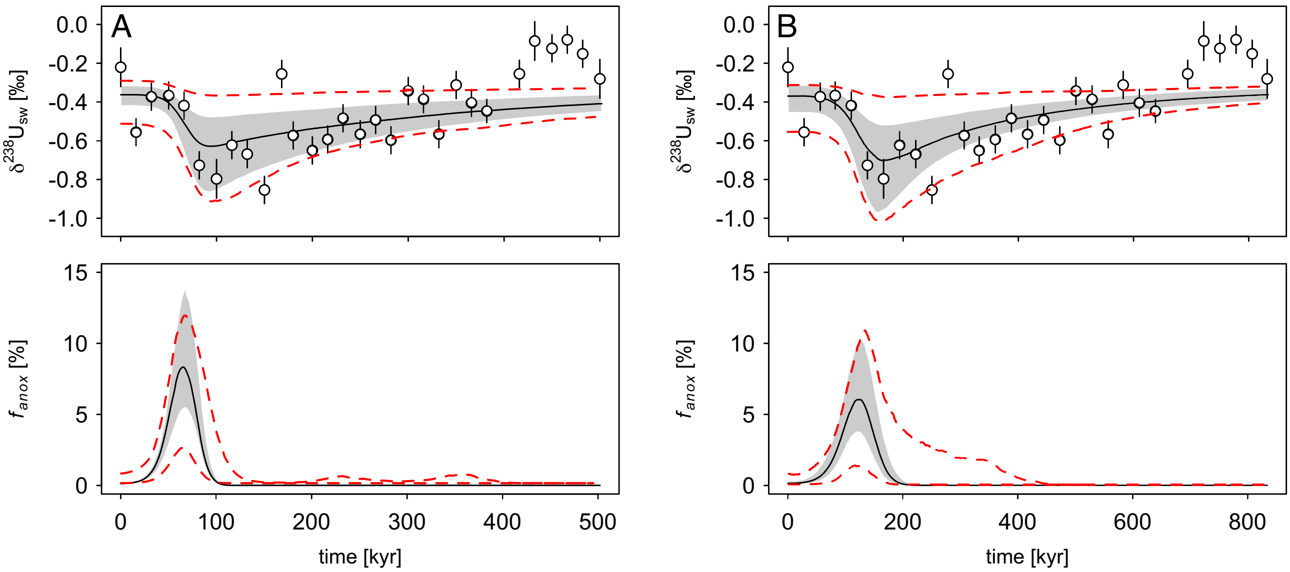

Fig. 3. Inversion results for seafloor anoxic area (f_{anox}) assuming (*A*) 300 kyr or (*B*) 500 kyr duration of the event. Black lines denote median; shading denotes 16th to 84th percentile CI using a uniform correction of −0.23‰ (39). Dashed red lines denote 16th to 84th percentile CI using a randomly distributed diagenetic offset of −0.23 ± 0.15‰ (the mean and 1 SD of ref. 39). SW = seawater. A shorter event implies a slightly greater expansion of seafloor anoxia to explain the magnitude of isotopic shift over the interval.

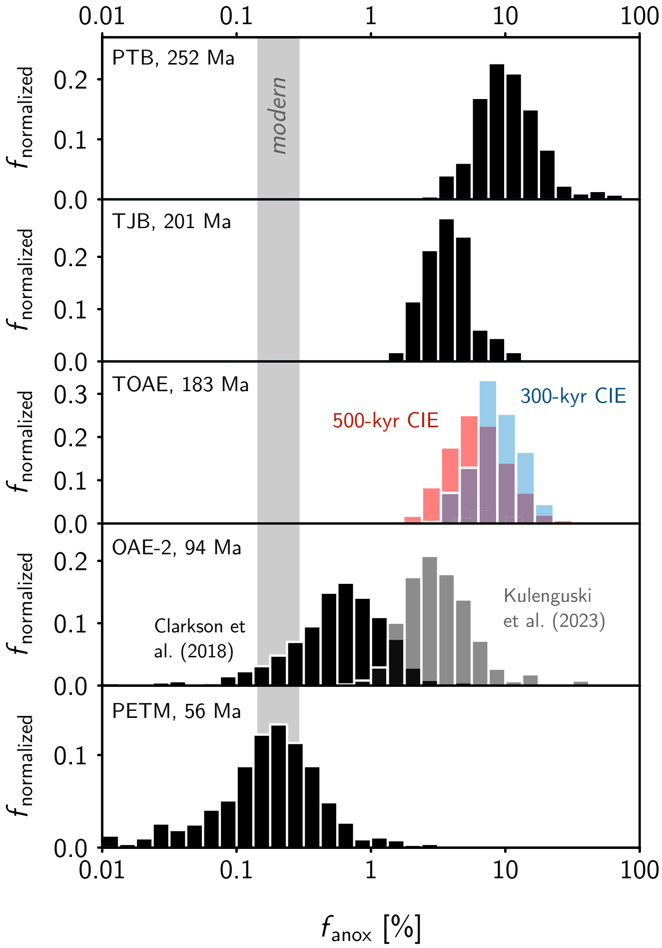

Fig. 4. Comparison of seafloor anoxic area (f_{anox}) modeled using $\delta^{238}U$ data for a variety of Phanerozoic OAEs. These include the Permo–Triassic boundary event (PTB, 252 Ma) (46), Triassic–Jurassic boundary event (TJB, 201 Ma) (42), T-OAE (183 Ma, this study), Cretaceous OAE 2 (OAE-2, 94 Ma) (43, 44), and the PETM (56 Ma) (45). Figure modified from ref. 39.

global seafloor and drives mass extinction of marine fauna. These scenarios from the geologic past are highly relevant for modern Earth as anthropogenic CO_2 release is already causing ocean deoxygenation (49) on an unprecedently rapid scale. Analogs from the geologic past such as the T-OAE may aid in predicting the timing and scale of future ocean deoxygenation, as well as its effect on the marine biosphere.

Materials and Methods

Analytical Methods. Thirty samples covering 39.2 m of strata were collected from the MSS section and crushed to a fine powder using an agate ball mill at the Potomac Science Center of George Mason University, taking care to avoid veins or other clear diagenetic features. Then, ~2 g of powder was reacted with 35 mL of 1M HNO_3 and 5 mL of concentrated HNO_3 overnight, followed by centrifugation and separation of the supernatant. All acids used in this study were trace metal grade. Following that, 200 µL of supernatant was then diluted with 9.8 mL of 2% HNO_3 and analyzed for a full suite of major, trace, and rare earth element abundances using a Thermo iCAP^{TM} quadrupole ICP-MS at Arizona State University. Typical precision is reported based on repeated analysis of simultaneously run standards, and in this study, relative percent s.d. was better than 6% for all reported elements. An amount of original solution containing 250 ng of U was then dried down and used for $\delta^{238}U$ analysis. $\delta^{238}U$ was determined using a $^{236}U/^{233}U$ double-spike (IRMM-3636) to correct for instrumental mass fractionation. Before column chemistry, 0.8 mL of a 10.7 ppb double-spike solution was added per 500 ng of U to achieve a U_{spike}/U_{sample} ratio of ~1.7% (50, 51). Samples were treated with reverse aqua regia (3:1 HNO_3:HCl), H_2O_2, and concentrated HNO_3 and ultimately redissolved in 3M HNO_3. Uranium was separated from matrix elements through ion-exchange chromatography using UTEVA resin. After column chemistry, samples were treated twice with concentrated HNO_3 and H_2O_2 to remove residual organics from the resin and then redissolved in 6M HNO_3. Samples were then subject to a second ion-exchange chromatography using DGA resin to remove excess Na that persists after UTEVA column chemistry. Ultimately, separated U was dissolved in 2% HNO_3 to a concentration of 40 ppb and analyzed for its isotopic composition using a Neptune Plus multicollector ICP-MS at the University of Maryland. The standard solution (CRM 145) was analyzed every two samples, with these values used to normalize sample $\delta^{238}U$ values via standard-sample bracketing. A second standard solution (CRM 129a) was analyzed after every ten analyses to ensure analytical reproducibility. The median $\delta^{238}U$ value we measured for CRM 129a is −1.72 ± 0.10‰ (2 SD), which is in good agreement with previous measurements in our lab (36, 52, 53). Precision of sample $\delta^{238}U$ values is reported as 2 SD of replicate measurements of the same sample solutions. Average precision for the sample set is ±0.10‰. We also assessed precision using the reproducibility of the bracketing standard CRM 145, which was also ±0.10‰ (2 SD, n = 42). The LOWESS fit through $\delta^{238}U$ data was constructed using a span that minimizes the corrected Akaike Information Criterion (54). The optimal span was chosen to be 0.7364 and the fit was implemented in the fANCOVA R package.

Geological Setting and Age Constraints. The MSS section is part of the thick shallow-marine carbonates of the ACP, which were deposited during the Late Triassic to the Late Cretaceous on the southern margin of the Tethys Ocean (54). The ACP was part of a system of carbonate platforms separated by deep basins which developed during the Mesozoic at subtropical latitudes at the margin of Adria (55, 56). The shallow-water carbonates of the ACP are now part of the southern Apennines fold-and-thrust belt (57), a segment of the orogenic system which formed by the convergence between the African and Eurasian continents, and rims most of the western Mediterranean Basin (58).

The average thickness of the ACP is about 5 km and covers a stratigraphic interval extending from the Upper Triassic to the Upper Cretaceous, representing nearly 150 Myr of shallow-marine carbonate sedimentation (59). The section studied in this paper comprises the Lower Jurassic *Palaeodasycladus* Limestones, named after the dasycladalean green alga *P. mediterraneus*, which is the most significant fossil, commonly reaching rock-forming abundance. The upper part of this unit is known as the Lithiotis Member, due to the great abundance of lithiotid bivalves, organized into large tabular biostromes (8, 31). The bivalve biostromes alternate with coarse-grained peloidal-intraclastic grainstones and rudstones with abundant remains of *P. mediterraneus*. The Lithiotis Member was deposited in an inner platform lagoon at very shallow-water depth, as indicated by the abundance of the bivalve genus *Mytiloperna* and of the dasycladalean algae (31). This unit is sharply overlain by the Oolitic Limestones, which consist of well-sorted grainstones deposited above fair-weather wave base. Overall, the whole studied section was deposited at very shallow depth, and there is no sedimentological evidence of restricted circulation nor of oxygen-poor conditions.

In Jurassic shallow-marine carbonates, it can be difficult to precisely define the chronostratigraphic ages due to the lack of fossils used as chronostratigraphic markers, such as ammonites and calcareous nannofossils. However, the age of the studied section has been constrained by integrating the available low-resolution biostratigraphy and chemostratigraphic correlation with well-dated deep-marine sections (*SI Appendix*, Fig. S3) (8). The extinction of *P. mediterraneus* can be confidently placed near the Pliensbachian-Toarcian boundary (60, 61). The Lithiotis Fauna is globally limited to the Pliensbachian-lower Toarcian (62), and its distribution reached a peak at the end of the Pliensbachian both in the classical area of the Trento Platform (63) and elsewhere in the western Tethys (62). The most significant feature of the carbon isotope profiles ($\delta^{13}C_{carb}$ and $\delta^{13}C_{org}$) of the studied section is a negative excursion starting at the boundary between the Lithiotis Member and Oolitic Limestones. The reliability of the carbon isotope record of the MSS section was evaluated and correlated with the n-CIE associated with the T-OAE in the reference sections of Peniche (Portugal) and Yorkshire (England; *SI Appendix*, Fig. S3), which both have detailed ammonite biostratigraphy and have been geochemically well characterized (8).

Also in the Adriatic Carbonate Platform, the onset of n-CIE associated with the T-OAE was documented just above the boundary between the Lithiotid Limestones and the "Spotted Limestones" (64) (*SI Appendix*, Fig. S3), mirroring the findings in the MSS section under study here (8) (*SI Appendix*, Fig. S3). The stratigraphic relation between the T-OAE n-CIE and the extinction of lithiotid bivalves has been documented also in the carbonate platform sections of the Tibetan Himalaya (65) and of the Central High Atlas (66). In conclusion, despite the inherent challenges of defining ages in shallow-water carbonates, we can confidently assign the n-CIE observed in the MSS section to the T-OAE n-CIE (8).

Modeling Methods. The δ^{238}U time series data were used to infer the most likely extent of seafloor anoxia (f_{anox}) through the T-OAE using the inverse isotope mass balance model of ref. 39. In brief, a Markov Chain Monte Carlo (MCMC) approach was used to optimize the fit of simulated δ^{238}U trajectories to the isotopic data. Convergence of the MCMC algorithm on the stationary distribution was assessed using trace plots and the Gelman–Rubin statistic, or potential scale reduction factor, for three or more parallel chains, each of which took $\geq 10^5$ steps. Upon converging on the optimized fit, uncertainty in the isotope mass balance was propagated by sampling published parameter ranges (appendix A in ref. 40 in 1,000 forward model realizations). Two inversion approaches were used. In the first approach, the measured δ^{238}U data were corrected for diagenetic alteration using a uniform correction of 0.23‰ (i.e., the average offset from seawater observed in modern Bahamian carbonates in ref. 39). These resulting time series are plotted (Fig. 3) with gray shading denoting the median and 16th to 84th percentile range of these model realizations. In the second approach, the diagenetic offset was randomly drawn from a normal distribution of 0.23 ± 0.15‰ (i.e., the mean and 1 SD of the ref. 39 dataset). The 16th to 84th percentile range of these model realizations is denoted with dashed red lines. The maximum extent of anoxia during the event was determined as the time bin during which the median reconstructed f_{anox} reached its highest value. Maximum f_{anox} is plotted as a histogram (Fig. 4), representing the inferred f_{anox} value for the 1,000 model realizations in the first approach described above.

Data, Materials, and Software Availability. All geochemical data generated here are publicly available at: https://zenodo.org/records/10638026 (67). Splits of samples are reposited at George Mason University and are available upon request.

ACKNOWLEDGMENTS. G.J.G. acknowledges funding from the College of Science at George Mason University. M.P. was partially funded by the MIUR under the project PRIN2017RX9XXXY. We thank David Paisley for laboratory assistance at George Mason University, as well as Tyler Goepfert and Trevor Martin for Quadrupole Inductively Coupled Plasma Mass Spectrometry assistance at Arizona State University.

Author affiliations: [a]Department of Atmospheric, Oceanic, and Earth Sciences, George Mason University, Fairfax, VA 22030; [b]Department of Geology and Earth System Science Interdisciplinary Center, University of Maryland, College Park, MD 20742; [c]Nicholas School of the Environment, Division of Earth and Climate Science, Duke University, Durham, NC 27708; [d]The Isotoparium, Division of Geological and Planetary Sciences, California Institute of Technology, Pasadena, CA 91125; and [e]Department of Earth Sciences, Environment and Resources, University of Naples Federico II, Naples 80126, Italy

1. H. C. Jenkyns, The early Toarcian (Jurassic) anoxic event; stratigraphic, sedimentary and geochemical evidence. *Am. J. Sci.* **288**, 101–151 (1988).
2. J. Pálfy, P. L. Smith, Synchrony between Early Jurassic extinction, oceanic anoxic event, and the Karoo-Ferrar flood basalt volcanism. *Geology* **28**, 747–750 (2000).
3. H. Svensen *et al.*, Hydrothermal venting of greenhouse gases triggering Early Jurassic global warming. *Earth Planet. Sci. Lett.* **256**, 554–566 (2007).
4. T. H. Heimdal, Y. Goddéris, M. T. Jones, H. H. Svensen, Assessing the importance of thermogenic degassing from the Karoo Large Igneous Province (LIP) in driving Toarcian carbon cycle perturbations. *Nat. Commun.* **12**, 6221 (2021).
5. M. N. Remírez, T. J. Algeo, Carbon-cycle changes during the Toarcian (Early Jurassic) and implications for regional versus global drivers of the Toarcian oceanic anoxic event. *Earth Sci. Rev.* **209**, 103283 (2020).
6. T. R. Bailey, Y. Rosenthal, J. M. McArthur, B. van de Schootbrugge, M. F. Thirlwall, Paleoceanographic changes of the Late Pliensbachian–Early Toarcian interval: A possible link to the genesis of an Oceanic Anoxic Event. *Earth Planet. Sci. Lett.* **212**, 307–320 (2003).
7. E. Mattioli, B. Pittet, G. Suan, S. Mailliot, Calcareous nannoplankton changes across the early Toarcian oceanic anoxic event in the western Tethys. *Paleoceanography* **23**, PA3208 (2008).
8. A. Trecalli, J. Spangenberg, T. Adatte, K. B. Föllmi, M. Parente, Carbonate platform evidence of ocean acidification at the onset of the early Toarcian oceanic anoxic event. *Earth Planet. Sci. Lett.* **357–358**, 214–225 (2012).
9. N. P. Ettinger *et al.*, Ocean acidification and photic-zone anoxia at the Toarcian Oceanic Anoxic Event: Insights from the Adriatic Carbonate Platform. *Sedimentology* **68**, 63–107 (2021).
10. M. N. Remírez, T. J. Algeo, Paleosalinity determination in ancient epicontinental seas: A case study of the T-OAE in the Cleveland Basin (UK). *Earth Sci. Rev.* **201**, 103072 (2020).
11. T. R. Them *et al.*, Evidence for rapid weathering response to climatic warming during the Toarcian Oceanic Anoxic Event. *Sci. Rep.* **7**, 5003 (2017).
12. W. Xu *et al.*, Evolution of the Toarcian (Early Jurassic) carbon-cycle and global climatic controls on local sedimentary processes (Cardigan Bay Basin, UK). *Earth Planet. Sci. Lett.* **484**, 396–411 (2018).
13. J. Fernández-Martínez *et al.*, Euxinia and hydrographic restriction in the Tethys Ocean: Reassessing global oceanic anoxia during the early Toarcian. *Glob. Planet. Change* **221**, 104026 (2023).
14. A. Kunert, B. Kendall, Global ocean redox changes before and during the Toarcian Oceanic Anoxic Event. *Nat. Commun.* **14**, 815 (2023).
15. G. Gambacorta, H.-J. Brumsack, H. C. Jenkyns, E. Erba, The early Toarcian Oceanic Anoxic Event (Jenkyns Event) in the Alpine-Mediterranean Tethys, north African margin, and north European epicontinental seaway. *Earth Sci. Rev.* **248**, 104636 (2024).
16. D. M. Raup, J. J. Sepkoski, Periodicity of extinctions in the geologic past. *Proc. Natl. Acad. Sci. U.S.A.* **81**, 801–805 (1984).
17. R. Vasseur *et al.*, Major coral extinctions during the early Toarcian global warming event. *Glob. Planet. Change* **207**, 103647 (2021).
18. C. V. Ullmann, N. Thibault, M. Ruhl, S. P. Hesselbo, C. Korte, Effect of a Jurassic oceanic anoxic event on belemnite ecology and evolution. *Proc. Natl. Acad. Sci. U.S.A.* **111**, 10073–10076 (2014).
19. F. J. Rodríguez-Tovar, Ichnology of the Toarcian Oceanic Anoxic Event: An understimated tool to assess palaeoenvironmental interpretations. *Earth Sci. Rev.* **216**, 103579 (2021).
20. V. Masson-Delmotte *et al.*, Eds., "Climate change 2021: The physical science basis" in *Contribution of Working Group I to the Sixth Assessment Report of the Intergovernmental Panel on Climate Change* (Cambridge University Press, 2021).
21. S. Boulila *et al.*, Astronomical calibration of the Toarcian Stage: Implications for sequence stratigraphy and duration of the early Toarcian OAE. *Earth Planet. Sci. Lett.* **386**, 98–111 (2014).
22. D. B. Kemp, G. Suan, A. Fantasia, S. Jin, W. Chen, Global organic carbon burial during the Toarcian oceanic anoxic event: Patterns and controls. *Earth Sci. Rev.* **231**, 104086 (2022).
23. A. J. Dickson *et al.*, Molybdenum-isotope chemostratigraphy and paleoceanography of the Toarcian Oceanic Anoxic Event (Early Jurassic). *Paleoceanography* **32**, 813–829 (2017).
24. C. R. Pearce, A. S. Cohen, A. L. Coe, K. W. Burton, Molybdenum isotope evidence for global ocean anoxia coupled with perturbations to the carbon cycle during the Early Jurassic. *Geology* **36**, 231 (2008).
25. T. R. Them *et al.*, Thallium isotopes reveal protracted anoxia during the Toarcian (Early Jurassic) associated with volcanism, carbon burial, and mass extinction. *Proc. Natl. Acad. Sci. U.S.A.* **115**, 6596–6601 (2018).
26. B. Kendall, M. B. Andersen, J. D. Owens, "Assessing the effect of large igneous provinces on global oceanic redox conditions using non-traditional metal isotopes (molybdenum, uranium, thallium)" in *Large Igneous Provinces*, (American Geophysical Union AGU, 2021), pp. 305–323.
27. T. R. Them II *et al.*, Reduced marine molybdenum inventory related to enhanced organic carbon burial and an expansion of reducing environments in the toarcian (early jurassic) oceans. *AGU Adv.* **3**, e2022AV000671 (2022).
28. J. M. McArthur, Early Toarcian black shales: A response to an oceanic anoxic event or anoxia in marginal basins? *Chem. Geol.* **522**, 71–83 (2019).
29. K. V. Lau, S. J. Romaniello, F. Zhang, *The Uranium Isotope Paleoredox Proxy* (*Elements in Geochemical Tracers in Earth System Science*, Cambridge University Press, 2019).
30. F. Zhang *et al.*, Uranium isotopes in marine carbonates as a global ocean paleoredox proxy: A critical review. *Geochim. Cosmochim. Acta* **287**, 27–49 (2020).
31. R. Posenato, D. Bassi, A. Trecalli, M. Parente, Taphonomy and evolution of Lower Jurassic lithiotid bivalve accumulations in the Apennine Carbonate Platform (southern Italy). *Palaeogeogr. Palaeoclimatol. Palaeoecol.* **489**, 261–271 (2018).
32. C. Korte, S. P. Hesselbo, Shallow marine carbon and oxygen isotope and elemental records indicate icehouse-greenhouse cycles during the Early Jurassic. *Paleoceanography* **26**, PA4219 (2011).
33. M. A. Kipp *et al.*, 238U, 235U and 234U in seawater and deep-sea corals: A high-precision reappraisal. *Geochim. Cosmochim. Acta* **336**, 231–248 (2022).
34. D. B. Cole *et al.*, Uranium isotope fractionation in non-sulfidic anoxic settings and the global uranium isotope mass balance. *Glob. Biogeochem. Cycles* **34**, e2020GB006649 (2020).
35. S. Bruggmann *et al.*, Uranium isotope cycling on the highly productive Peruvian margin. *Chem. Geol.* **590**, 120705 (2022).
36. R. L. Rutledge *et al.*, Productivity and organic carbon loading control uranium isotope behavior in ancient reducing settings: Implications for the paleoredox proxy. *Geochim. Cosmochim. Acta* **368**, 197–213 (2024), 10.1016/j.gca.2024.01.007.
37. K. V. Lau *et al.*, Variable local basin hydrography and productivity control the uranium isotope paleoredox proxy in anoxic black shales. *Geochim. Cosmochim. Acta* **317**, 433–456 (2022).
38. X. Chen *et al.*, Diagenetic effects on uranium isotope fractionation in carbonate sediments from the Bahamas. *Geochim. Cosmochim. Acta* **237**, 294–311 (2018).
39. F. L. H. Tissot *et al.*, Controls of eustasy and diagenesis on the 238U/235U of carbonates and evolution of the seawater (234U/238U) during the last 1.4 Myr. *Geochim. Cosmochim. Acta* **242**, 233–265 (2018).
40. M. A. Kipp, F. L. H. Tissot, Inverse methods for consistent quantification of seafloor anoxia using uranium isotope data from marine sediments. *Earth Planet. Sci. Lett.* **577**, 117240 (2022).
41. M. Pimentel-Galvan *et al.*, Duration and intensity of end-permian marine anoxia. *Geochem. Geophys. Geosystems* **23**, e2021GC010130 (2022).
42. A. B. Jost *et al.*, Uranium isotope evidence for an expansion of marine anoxia during the end-Triassic extinction. *Geochem. Geophys. Geosystems* **18**, 3093–3108 (2017).
43. M. O. Clarkson *et al.*, Uranium isotope evidence for two episodes of deoxygenation during Oceanic Anoxic Event 2. *Proc. Natl. Acad. Sci. U.S.A.* **115**, 2918–2923 (2018).
44. M. O. Clarkson *et al.*, Upper limits on the extent of seafloor anoxia during the PETM from uranium isotopes. *Nat. Commun.* **12**, 399 (2021).
45. F. Zhang *et al.*, Congruent Permian-Triassic δ238U records at Panthalassic and Tethyan sites: Confirmation of global-oceanic anoxia and validation of the U-isotope paleoredox proxy. *Geology* **46**, 327–330 (2018).

46. R. Bartlett *et al.*, Abrupt global-ocean anoxia during the Late Ordovician–early Silurian detected using uranium isotopes of marine carbonates. *Proc. Natl. Acad. Sci. U.S.A.* **115**, 5896–5901 (2018).
47. D. A. White, M. Elrick, S. Romaniello, F. Zhang, Global seawater redox trends during the Late Devonian mass extinction detected using U isotopes of marine limestones. *Earth Planet. Sci. Lett.* **503**, 68–77 (2018).
48. F. Zhang *et al.*, Extensive marine anoxia associated with the Late Devonian Hangenberg Crisis. *Earth Planet. Sci. Lett.* **533**, 115976 (2020).
49. A. Oschlies, P. Brandt, L. Stramma, S. Schmidtko, Drivers and mechanisms of ocean deoxygenation. *Nat. Geosci.* **11**, 467–473 (2018).
50. S. Weyer *et al.*, Natural fractionation of 238U/235U. *Geochim. Cosmochim. Acta* **72**, 345–359 (2008).
51. G. J. Gilleaudeau *et al.*, Uranium isotope evidence for limited euxinia in mid-Proterozoic oceans. *Earth Planet. Sci. Lett.* **521**, 150–157 (2019).
52. J. T. Kulenguski *et al.*, Carbonate uranium isotopes across Cretaceous OAE 2 in southern Mexico: New constraints on the global spread of marine anoxia and organic carbon burial. *Palaeogeogr. Palaeoclimatol. Palaeoecol.* **628**, 111756 (2023).
53. L. B. Cherry *et al.*, A diverse Ediacara assemblage survived under low-oxygen conditions. *Nat. Commun.* **13**, 7306 (2022).
54. A. Bosellini, The Western passive margin of Adria and its carbonate platforms. *Spec. Vol. Ital. Geol. Soc. IGC* **32**, 79–92 (2004).
55. J. E. T. Channell, B. D'Argenio, F. Horváth, Adria, the African promontory, in mesozoic Mediterranean palaeogeography. *Earth Sci. Rev.* **15**, 213–292 (1979).
56. G. Stampfli, J. Mosar, The making and becoming of Apulia. *Mem. Sci. Geol.* **51**, 141–154 (1999).
57. S. Vitale, S. Ciarcia, Tectono-stratigraphic and kinematic evolution of the southern Apennines/Calabria–Peloritani Terrane system (Italy). *Tectonophysics* **583**, 164–182 (2013).
58. L. Royden, C. Faccenna, Subduction orogeny and the late cenozoic evolution of the Mediterranean Arcs. *Annu. Rev. Earth Planet. Sci.* **46**, 261–289 (2018).
59. M. Parente, S. Amodio, A. Iannace, M. Sabbatino, Stratigraphy and facies of the Apennine Carbonate Platform (southern Italy): The record of Mesozoic OAEs and Miocene transgression. *Geol. Field Trips* **14**, 1–75 (2022).
60. J.-P. Bassoullet, Distribution des principales especes. *Biostratigraph. Jurassique Ouest-Eur. Méditerr.* **17**, 339–341 (1997).
61. F. Barattolo, R. Romano, Anonymous, Shallow carbonate platform bioevents during the Upper Triassic-Lower Jurassic; an evolutive interpretation. *Ital. J. Geosci.* **124**, 123–142 (2005).
62. N. M. Fraser, D. J. Bottjer, A. G. Fischer, Dissecting "Lithiotis" Bivalves: Implications for the Early Jurassic Reef Eclipse. *PALAIOS* **19**, 51–67 (2004).
63. M. Franceschi *et al.*, Early Pliensbachian (Early Jurassic) C-isotope perturbation and the diffusion of the Lithiotis Fauna: Insights from the western Tethys. *Palaeogeogr. Palaeoclimatol. Palaeoecol.* **410**, 255–263 (2014).
64. N. Sabatino *et al.*, Carbon-isotope record and palaeoenvironmental changes during the early Toarcian oceanic anoxic event in shallow-marine carbonates of the Adriatic Carbonate Platform in Croatia. *Geol. Mag.* **150**, 1085–1102 (2013).
65. Z. Han, X. Hu, D. B. Kemp, J. Li, Carbonate-platform response to the Toarcian Oceanic Anoxic Event in the southern hemisphere: Implications for climatic change and biotic platform demise. *Earth Planet. Sci. Lett.* **489**, 59–71 (2018).
66. F.-N. Krencker *et al.*, Two-phased collapse of the shallow-water carbonate factory during the late Pliensbachian-Toarcian driven by changing climate and enhanced continental weathering in the Northwestern Gondwana Margin. *Earth Sci. Rev.* **208**, 103254 (2020).
67. G. J. Gilleaudeau, Mercato San Severino T-OAE uranium isotope dataset. Zenodo. https://zenodo.org/records/10638026. Deposited 9 February 2024.